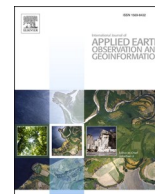




Contents lists available at ScienceDirect

# International Journal of Applied Earth Observations and Geoinformation

journal homepage: [www.elsevier.com/locate/jag](http://www.elsevier.com/locate/jag)

## Remote sensing of chlorophyll-*a* concentrations in coastal oceans of the Greater Bay Area in China: Algorithm development and long-term changes

Yan Tong<sup>a</sup>, Lian Feng<sup>a,\*</sup>, Dan Zhao<sup>a</sup>, Wang Xu<sup>b</sup>, Chunmiao Zheng<sup>a</sup><sup>a</sup> School of Environmental Science and Engineering, Southern University of Science and Technology, Shenzhen, China<sup>b</sup> Shenzhen Ecological and Environmental Monitoring Center of Guangdong Province, Shenzhen, China

## ARTICLE INFO

## Keywords:

Chlorophyll-*a*  
Coastal Ocean  
OC3  
Hybrid Algorithm  
Greater Bay Area

## ABSTRACT

Extensive human activities and climate change in recent decades have triggered severe eutrophication problems in the coastal oceans in the Greater Bay Area (GBA) of China. However, a comprehensive characterization of the spatial and temporal patterns of chlorophyll-*a* (Chl-*a*, a major indicator of phytoplankton biomass) in this region is not available. Our study attempts to fill this gap by using long-term satellite observations. With massive *in situ* datasets from underway sampling systems, we developed a novel hybrid Chl-*a* retrieval algorithm combining the recalibrated OC3 and line-height-based (BL443) algorithms for waters with different turbidity levels. Satellite-retrieved Chl-*a* values with the hybrid algorithm agreed well with *in situ* measurements, with an uncertainty level of 33.8%. Long-term analysis revealed significant decreasing trends over the inner Pearl River Estuary (averaged at 0.054  $\mu\text{g/L yr}^{-1}$ ), while significant increasing trends were found in eastern Daya Bay (averaged at 0.035  $\mu\text{g/L yr}^{-1}$ ). The developed algorithm is expected to aid routine Chl-*a* monitoring in the adjacent oceans of the GBA, and the long-term datasets here can serve as critical information for further coastal conservation and management efforts.

### 1. Introduction

In recent decades, global coastal regions have been threatened by continuous inputs of large amounts of nutrients and contaminants from adjacent watersheds (Breitburg et al., 2018). These threats will likely intensify marine environmental issues due to foreseeable terrestrial nutrient inputs from population growth and urbanization development in the future (Neumann et al., 2015). Nutrient inputs contribute to ecosystem degradation, such as bottom-water hypoxia (Breitburg et al., 2018; Li et al., 2020; Lu et al., 2018) and red tides or harmful algal blooms (Stokal et al., 2014). Such issues could be exacerbated by complex physico-hydrodynamic and biogeochemical processes as well as climatic warming.

Chlorophyll-*a* (Chl-*a*) is the principal pigment in phytoplankton, and its concentration (in  $\mu\text{g/L}$ ) has been commonly used as a proxy for biomass and primary production (Boyce et al., 2010). Chl-*a* concentration serves as the primary indicator to evaluate the eutrophication status of oceanic waters (Gohin et al., 2019), and it has also been considered an essential input for geophysical and geochemistry models used to understand how the oceans respond to climate changes and human activities (Lu et al., 2018; Lu et al., 2020; Ning et al., 2004). Traditionally,

Chl-*a* datasets were obtained through ship-based sampling methods, whereas the limited spatial coverage and observational frequency make it challenging to capture the highly dynamic and heterogeneous features of Chl-*a* in estuarine waters (Cheng et al., 2020). However, such limitations do not apply to satellite remote sensing; synoptic and frequent observations make it useful to examine short- to long-term changes in Chl-*a* in global or regional oceanic waters.

Unfortunately, the Chl-*a* retrieval algorithms based on remote sensing data developed for one specific coastal region may not apply to others due to the potential disparities in the optical properties of water (Arabi et al., 2020; Gitelson et al., 2007). This problem is particularly true for estuarine waters, where clean oceanic saltwater and turbid riverine freshwater mix constantly, and the strength and extent of the mixing vary in different seasons and positions. Such a disturbing effect results in high turbidity with high seasonal and spatial variations, making water optically complex and challenging the development of a robust Chl-*a* algorithm (Xiong and Liu, 2018). One typical example is the Pearl River Estuary (PRE) in China, where discharge ranks second in China and 13th in the world and presents remarkable seasonal differences. Surrounding the PRE is the Greater Bay Area (GBA), which covers nine large cities in the Guangdong Province and two special

\* Corresponding author at: School of Environmental Science and Engineering, Southern University of Science and Technology, Shenzhen, China.

E-mail address: [fengl@sustech.edu.cn](mailto:fengl@sustech.edu.cn) (L. Feng).

<https://doi.org/10.1016/j.jag.2022.102922>

Received 6 November 2021; Received in revised form 8 July 2022; Accepted 13 July 2022

Available online 4 August 2022

1569-8432/© 2022 Published by Elsevier B.V. This is an open access article under the CC BY-NC-ND license (<http://creativecommons.org/licenses/by-nc-nd/4.0/>).

administrative regions (i.e., Hong Kong and Macau) and represents one of the most populated regions worldwide. A series of environmental consequences on the coast of the GBA has been triggered by continuously extensive human activities and the associated enrichments in nutrients and pollutants (Hu et al., 2001; Wang et al., 2008; Wu et al., 2018; Xuan et al., 2020). For example, red tides have been frequently reported in the PRE during recent decades (e.g., Qiu et al., 2019; Xuan et al., 2020), further causing extensive ecosystem consequences, such as fish death and hypoxia (Breitburg et al., 2018; Li et al., 2020). However, before effective management policies can be initiated to mitigate estuarine environments, accurate assessments of the historical and current water quality conditions are required.

Many previous studies have attempted to develop remote sensing algorithms for Chl-*a* mapping in the coastal waters of the GBA, with a particular focus on the PRE (Chen et al., 2011; Fu et al., 2015; Hafeez et al., 2019; Liu et al., 2008; Liu et al., 2010; Liu and Tang, 2019; Nazeer and Nichol, 2016; Zhang et al., 2011; Zhang et al., 2009). However, all previous attempts were either focused on Chl-*a* algorithm development with a few field samples collected in limited days and seasons, or only sporadic remote sensing images were used to examine the overall patterns of Chl-*a* spatial distributions. In other words, the current Chl-*a* regional algorithms are not applicable for long-term remote sensing images covering water in different seasons and with varying optical components, and previous remote sensing-based observations provided insufficient information on Chl-*a* patterns within this region. Fortunately, since 1986 the Hong Kong Environmental Protection Department (HKEPD) has conducted routine *in situ* samplings and thus made it possible to understand the long-term Chl-*a* dynamics of the PRE (Yung

et al., 2001; Zhang et al., 2018). However, their sampling frequency (one cruise per month) and spatial coverage (only covering the coastal oceans of Hong Kong Island, see Fig. 1) prevent their accurate characterization of Chl-*a* overall adjacent oceans in the GBA. As such, the eutrophication status of the majority of the coastal waters in the GBA is unknown.

Motivated by the absence of comprehensive documentation of the Chl-*a* patterns over the coastal oceans in the GBA, this study is designed with the following objectives: (1) develop a novel Chl-*a* algorithm using a large volume of *in situ* measurements collected by underway sampling systems and further determine its accuracy levels; (2) map the long-term spatial and temporal Chl-*a* distributions in coastal oceans of the GBA using all available Moderate-resolution Imaging Spectroradiometer (MODIS) images between 2003 and 2019.

## 2. Study area and datasets

### 2.1. Study area

The GBA represents the areas around the Pearl River Estuary (PRE), which is located in southeastern China (see Fig. 1). The water discharge from the Pearl River flows into the ocean through eight large outlets of the PRE and exhibits substantial seasonality, with ~80% of the annual total water discharge occurring in wet seasons (April to September) (Harrison et al., 2008; Wang et al., 2021). Coupled with riverine discharge, many physical factors such as wind and tide also contribute to the regional hydrodynamic characteristics (Wong et al., 2003). Located on the right side of the PRE are two semi-enclosed bays (i.e., Daya Bay (DYB) and Dapeng Bay (DPB), see Fig. 1), where the water exchanges

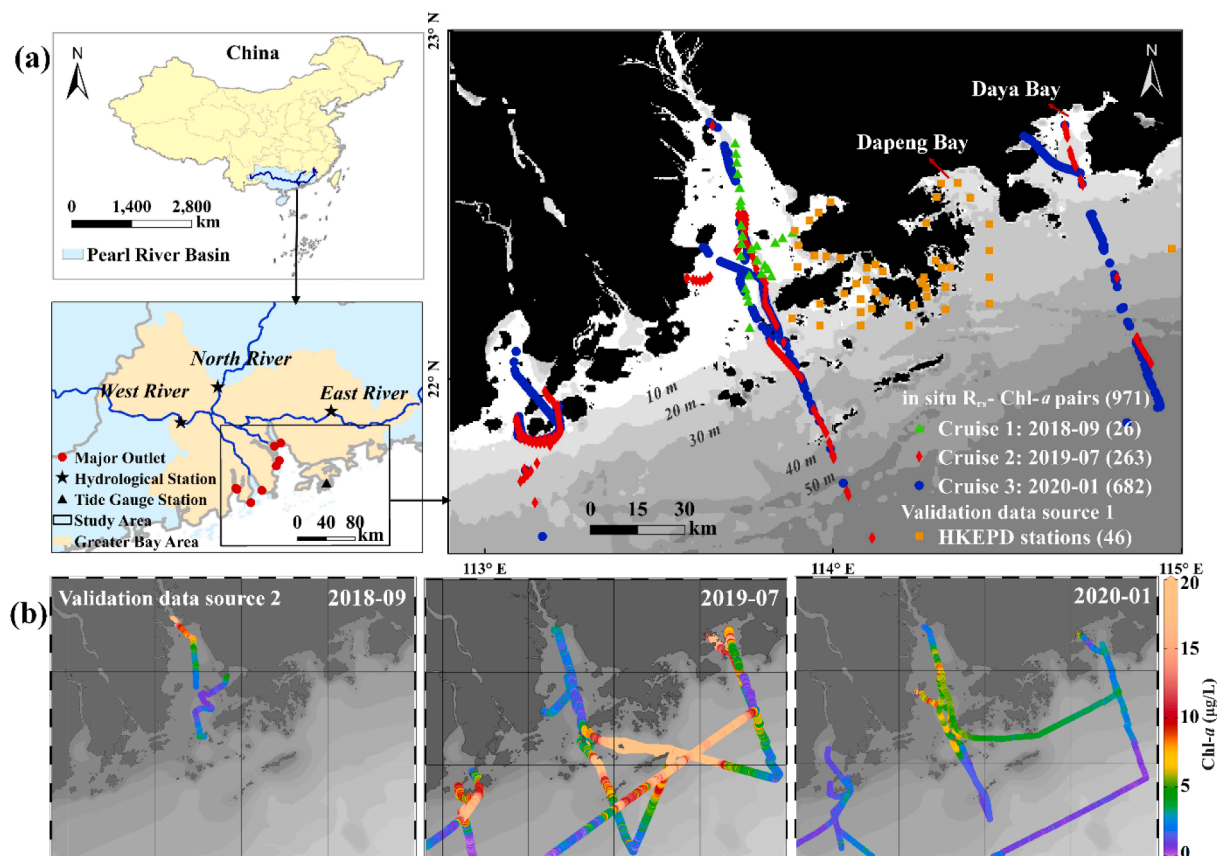


**Fig. 1.** (a) Maps of the study area and its association with the Greater Bay Area and Pearl River Basin. The three main tributaries (blue lines), hydrological stations (black stars), tide gauge stations (black triangles), and eight large outlets (red circles) are indicated on the map. The locations of *in situ* Chl-*a* and  $R_{rs}$  match-up pairs and their sampling months as well as the bathymetric contour are also indicated; the numbers of pairs are annotated in the parenthesis of the legend. The routine HKEPD sampling sites (yellow squares) are also illustrated. (b) Tracks of three field cruises, where the Chl-*a* values (μg/L) were collected by the underway sampling system, are color-coded.

constantly with the South China Sea without large river discharge (Wang et al., 2008). The GBA has the highest rates of urbanization and industrialization in China; the regional GDP and population account for 12% and 5% in China, respectively (Zhang et al., 2020). However, due to rapid urbanization and climatic change, water quality adjacent to the coastal area is under threat of degradation. One of the most concerning issues is frequent red tides, although the affected area and frequency have been declining according to the annual Marine Environmental Quality Bulletin of Guangdong Province, as shown in Figure S1.

## 2.2. In situ data

Three field cruises in September 2018, July 2019, and January 2020 were conducted to obtain *in situ* data in the study region (Fig. 1a), where water quality parameters (Chl-*a* and turbidity) and remote sensing reflectance ( $R_{rs}$ ) were measured. Datasets were automatically collected through integrated underway sampling systems developed by Sinofloat Co., Ltd., including an apparent optical property (AOP) observation system (GZSS\_CruiseAOP) and a bio-optical parameter observation system (ZKQH\_CruiseBOP) (see specifications for the two systems in Table S1). The GZSS\_CruiseAOP system has three hyperspectral radiometers (TriOS RAMSES), measuring the above-water upwelling radiance ( $L_u$ ), the skylight radiance ( $L_{sky}$ ) and the downwelling irradiance ( $E_d$ ), respectively, in a simultaneous manner (Fig. 2a). The  $R_{rs}$  data for each measurement were estimated as follows:

$$R_{rs} = \frac{L_u - \rho_f \times L_{sky}}{E_d} \quad (1)$$

where  $\rho_f$  is the sea surface reflectance factor, which was set to 0.028 (Mobley, 1999). *In situ* hyperspectral  $R_{rs}$  measurements were converted into equivalent MODIS bands with the spectral response functions of MODIS instruments before their use in algorithm development and evaluation (Li et al., 2019).

The ZKQH\_CruiseBOP system configured an ECO-Triplet instrument

(WET Labs, 2008) within a sealed tank; surface water is constantly pumped into the tank along the cruise track to measure the Chl-*a* and turbidity data every 15 s, based on the fluorescence of chlorophyll and backscattering of sediments, respectively (Fig. 2b). Bubbles within the tank were removed first through a prefiltering device to exclude potential impacts on data quality. Furthermore, sporadic water samples at the ocean surface were collected during the cruise surveys when possible. The samples were taken into the laboratory to measure the concentrations of Chl-*a* and total suspended sediments (TSS), following the same methods used in Guan et al. (2020). Indeed, the underway Chl-*a* (or turbidity) measurements are highly correlated with laboratory-measured Chl-*a* (or TSS) (see Fig. 3), indicating the high reliability of the datasets collected by the ZKQH\_CruiseBOP system. Therefore, the relationships presented in Fig. 3 were used to recalibrate the underway measurements of the ZKQH\_CruiseBOP system.

Datasets collected from the two underway systems (i.e., Chl-*a*- $R_{rs}$  pairs) at the same time and location were determined, and the quality assurance (QA) screening criteria were applied to exclude low-quality  $R_{rs}$  measurements (Wei et al., 2016). A total of 971 Chl-*a*- $R_{rs}$  pairs were obtained (see locations in Fig. 1a), covering 19 days during the three cruises. The  $R_{rs}$  spectra and Chl-*a* concentrations for these pairs are plotted in Fig. 2c&d, and the associated statistics are listed in Table 1. *In situ* Chl-*a*- $R_{rs}$  match-ups (Fig. 1a, 971 samples) and all high-frequency Chl-*a* measurements during the three cruises were used to calibrate and validate the Chl-*a* estimation algorithms.

*In situ* Chl-*a* data of Hong Kong coastal waters were also routinely measured at three depths (surface, middle, and bottom) based on a spectro-photometric method by the HKEPD (<https://www.epd.gov.hk/>) on a monthly basis starting in 1986, which serve as valuable independent datasets to gauge the performance of the satellite-derived Chl-*a* concentrations. Long-term surveyed data from 46 HKEPD stations (see yellow squares in Fig. 1a) were obtained, where the stations are located at least three MODIS pixels away from the coastline to eliminate potential impacts of land adjacent effects on the Chl-*a* retrievals (Feng and

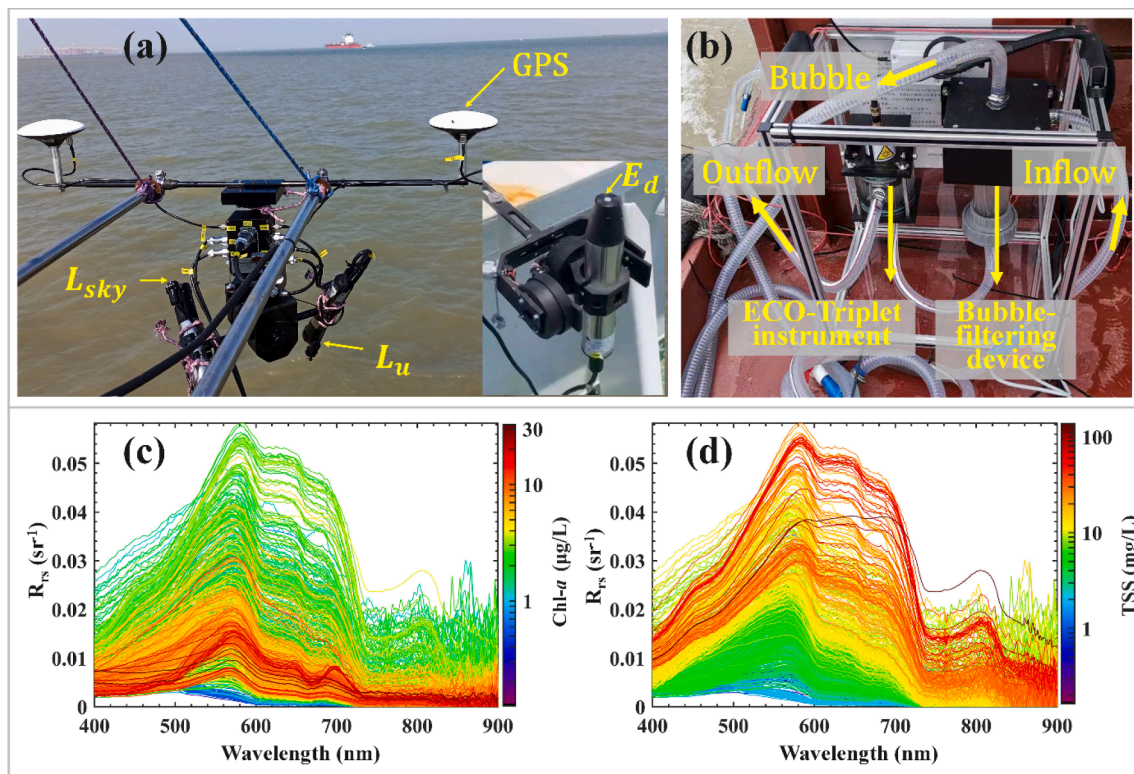


Fig. 2. Photographs of the underway (a) apparent optical property observation system (GZSS\_CruiseAOP) and (b) bio-optical parameter observation system (ZKQH\_CruiseBOP).  $R_{rs}$  spectral measurements color-coded according to their Chl-*a* (c) and TSS (d) concentrations.

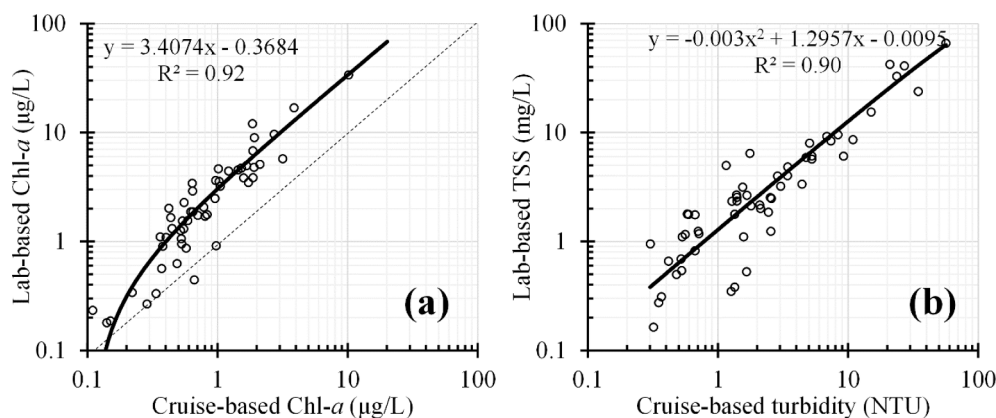


Fig. 3. Relationship between laboratory-based and cruise-based water quality. (a) Chl-a ( $R^2 = 0.92$ ) and (b) TSS ( $R^2 = 0.90$ ).

Table 1

Statistics of *in situ* Chl-*a* and TSS concentrations collected during three cruises.

Cruise	N	Chl- <i>a</i> (µg/L)				TSS (mg/L)			
		max	min	mean ± STD	median	max	min	mean ± STD	median
2018-09	26	8.34	0.49	2.31 ± 1.84	1.49	137.50	1.21	23.08 ± 29.66	11.02
2019-07	263	32.74	0.13	5.93 ± 4.60	4.85	66.05	0.16	9.72 ± 11.78	5.18
2020-01	682	12.70	0.22	3.12 ± 2.17	2.27	41.19	0.35	6.53 ± 6.26	4.03
Total	971	32.74	0.13	3.80 ± 3.23	2.85	137.50	0.16	7.82 ± 9.97	4.65

Hu, 2017). In total, Chl-*a* measurements from 12,765 samples were obtained between 2003 and 2019 (Fig. 1a).

### 2.3. MODIS data and preprocessing

Level 1A MODIS/Aqua images covering the study area were downloaded from the NASA Goddard Space Flight Center (GSFC, <https://oceancolor.gsfc.nasa.gov/>), and a total of 5879 images from 2003 to 2019 were obtained. These images were processed with SeaDAS software (version 7.4) to produce  $R_{rs}$  data using the NIR-SWIR-based atmospheric correction algorithm (Wang and Shi, 2006). The NIR-SWIR algorithm was specifically designed for productive coastal and inland waters, and extensive validations have demonstrated its high performance in global and regional oceans (Vanhellemont and Ruddick, 2015; Wang and Shi, 2007; Wang et al., 2009; Xu et al., 2020). Notably, the default cloud albedo mask was changed from  $R_{rc,869} = 0.027$  to  $R_{rc,2130} = 0.037$  ( $R_{rc,869}$  and  $R_{rc,2130}$  are the Rayleigh scattering corrected reflectance of MODIS bands at 869 nm and 2130 nm, respectively), which is used to obtain more valid satellite observations on the turbid coast; this practice was also recommended by previous studies (Wang et al., 2021; Wang and Shi, 2006). The  $R_{rs}$  images were remapped to a cylindrical equidistance projection and then resampled to a spatial resolution of 250 m. Sensitivity analysis revealed that the resampling process presented small impact on Chl-*a* maps, with mean absolute bias of 0.02 µg/L (1%) and mean ratio of 0.97. Furthermore, we applied the QA screening criteria proposed by Wei et al. (2016) to remove invalid pixels (i.e., QA score < 0.5).

## 3. Methods

### 3.1. Chl-*a* algorithm development

Various remote sensing algorithms have been proposed previously to estimate Chl-*a* in oceanic and inland waters, which can be classified as either empirical or semianalytical algorithms (e.g., Matthews, 2011; Neil et al., 2019; Odermatt et al., 2018; Odermatt et al., 2012). In general, empirical algorithms are based on correlations between Chl-*a* and certain band combinations (i.e., spectral indices) of remote sensing

instruments, while semianalytical algorithms require physical modeling of in-water radiometric transfer processes (i.e., absorption and scattering). We selected many spectral indices that have been successful for Chl-*a* estimations in global or regional oceanic waters, aiming to find the optimal index for our study region (see Table 2). These indices are categorized into four different types, including blue-green (e.g., OC3, O'Reilly and Werdell, 2019), green-red (e.g., Le et al., 2013), red-NIR (e.g., Gitelson et al., 2008), and baseline (e.g., CI, Hu et al., 2012; FLH, Letelier and Abbott, 1996; MCI, McCullough, 2007; SCI, Shen et al., 2010). Each of the first three types of spectral indices may involve various forms, such as the difference-based and ratio-based forms for blue-green, three-band, or four-band-based forms for red-NIR. However, we found a similar performance (not shown here) among different forms in each type and thus only listed a single form for each type (i.e., blue-green, green-red, red-NIR) in Table 2.

We used *in situ*  $R_{rs}$ -Chl-*a* pairs to recalibrate the correlations between different spectral indices and Chl-*a* and then calculated the accuracy measures using *in situ*  $R_{rs}$ -estimated and field-measured Chl-*a* (see below). Furthermore, we explored the impact of turbidity on these algorithms by using  $R_{rs,645}$  as a proxy for turbidity levels (see Fig. 4). In practice, we used  $R_{rs}$ -Chl-*a* pairs where  $R_{rs,645}$  was below a certain threshold (denoted as  $Thres-R_{rs,645}$ ) to perform the recalibration and performance evaluation procedures (Fig. 4a, b). Then, we determined the optimal algorithm and its applicable turbidity levels (i.e.,  $R_{rs,645}$ ) by examining the responses of the accuracy measures to different  $Thres-R_{rs,645}$ . Indeed, the magnitude of  $R_{rs,645}$  has been widely used for turbidity retrievals in coastal and inland waters (Hu et al., 2004; Ondrusek et al., 2012) because of the strong scattering of suspended sediments and the relatively small signal from other optically sensitive components (i.e., Chl-*a* and CDOM) in the red band. Moreover, we evaluated the performance of the quasi-analytical algorithm (QAA) developed by Lee et al. (2002) for retrieving Chl-*a* by using all the *in situ*  $R_{rs}$ -Chl-*a* pairs.

To address the poor performances of these previously used spectral indices in obtaining Chl-*a* in highly turbid waters (Fig. 4a, b), a regionalized spectral index with a better correlation with Chl-*a* in the study area is proposed. We tested the correlation relationship between Chl-*a* and all possible combinations of MODIS bands (see correlation

**Table 2**  
Performances of frequently used Chl-a algorithms for low-turbid waters ( $R_{rs,645} < 0.006$ ,  $N = 373$ ).

Combination forms	model	Reference	Spectral indices	$R^2$	$R^2(\log)$	MRD (%)	URMSD (%)	MedRatio
Blue-Green	OC3	O'Reilly and Werdell, 2019	$\max(R_{rs}(443), R_{rs}(488))/R_{rs}(547)$	0.47	0.73	30.27	32.66	0.98
Green-Red	GR2	Le et al., 2013	$R_{rs}(667)/R_{rs}(547)$	0.14	0.20	45.04	51.17	1.15
Red-NIR	RN3	Gitelson et al., 2008	$(1/R_{rs}(645) - 1/R_{rs}(678)) \times R_{rs}(748)$	0.06	0.12	57.93	59.63	1.41
CI	CI	Hu et al., 2012	BL (443,555,667)*	0.10	0.47	47.19	50.13	0.97
FLH	FLH	Letelier and Abbott, 1996	BL (667,678,748)	0.23	0.51	51.80	49.86	1.33
MCI	MCI	McCullough, 2007	BL (645,748,859)	0.04	0.19	58.23	58.49	1.36
SCI	SCI	Shen et al., 2010	SCI (555,645,667,678)**	0.00	0.05	61.13	59.26	1.41
Semianalytical model <sup>§</sup>	QAA	Lee et al., 2002		0.47	0.38	43.49	45.77	1.18

\*BL (b1, b2, b3) indicates  $R_{rs,b2} - (R_{rs,b1} + (b2 - b1)/(b3 - b1) \times (R_{rs,b3} - R_{rs,b1}))$ .  
\*\*SCI (b1, b2, b3, b4) indicates  $-BL(b4, b3, b2) - BL(b4, b2, b1)$ .

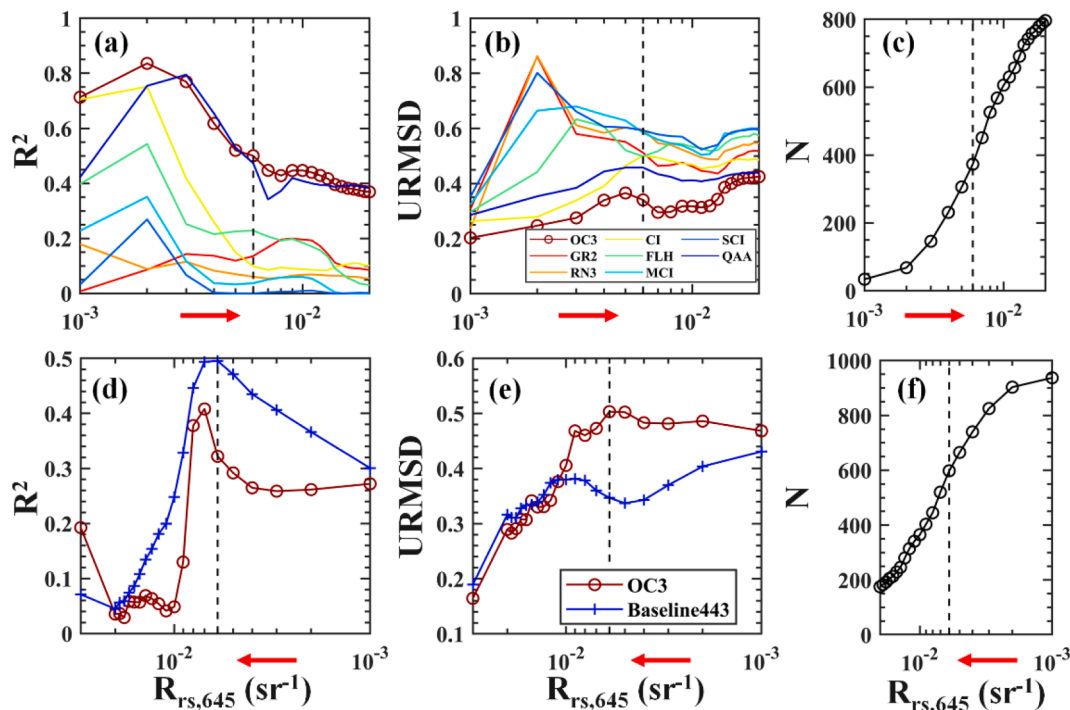


**Fig. 4.** (a-b) Performance comparison between OC3 and seven commonly used models under increasing turbidity levels (represented by increased  $R_{rs,645}$ ). (d-e) Performance of the BL443 model and OC3 algorithm under decreasing turbidity levels (represented by decreased  $R_{rs,645}$ ). (c-f) The cumulative number of samples for their corresponding left panels.

coefficients in Table 3) to develop an algorithm that is applicable to highly turbid waters in this region. Similar to the procedures for low-turbidity waters, we also examined the sensitivity of these algorithms at different turbidity levels (represented as  $R_{rs,645}$ ). In this case, we used *in situ*  $R_{rs}$ -Chl-a pairs when  $R_{rs,645}$  was above various thresholds to calibrate and validate these algorithms (see Fig. 4d, e), and we determined both the optimal algorithm and the applicable turbidity level.

### 3.2. Algorithm validations

To determine the accuracy levels of the developed Chl-a algorithm, satellite-derived Chl-a data were compared against concurrently measured Chl-a datasets from both the HKEPD (13,150 in total) and our cruise surveys (56,167 in total, not used in  $R_{rs}$ -Chl-a pairs). Several criteria were followed when determining concurrent satellite-*in situ* match-up pairs: (1) the *in situ* measurements and satellite overpasses are within 3 h a day for the cruise survey data obtained by our group; such a

time window was set to 1 day for the HKEPD datasets since the time information was not available; and (2) > 50 % (i.e.,  $\geq 5$ ) of the pixels within the  $3 \times 3$ -pixel window centered at each *in situ* station are valid (i.e., spectra can pass the QA screening mentioned above), where the coefficient of variation (calculated as the standard deviation divided by the mean) is < 5 % within the window. Then, the median Chl-a of the valid pixels within a  $3 \times 3$  window was calculated to represent satellite retrieval. A total of 255 satellite-*in situ* match-up pairs were obtained, and the data were spread across different seasons. Note that one major reason to include the HKEPD dataset in our study is that few satellite-*in situ* match-up pairs at low-turbidity levels were obtained from our survey data.

The accuracy measures used to determine the agreements between Chl-a estimates (both from *in situ* spectra and satellite) and field measurements include slope, coefficient of determination ( $R^2$ ), the median relative difference (MRD, %), unbiased root median squared relative difference (URMSD, %), and median ratio (MedRatio). The use of

**Table 3**

Spectral combination forms previously proposed for Chl-*a* estimation. For each form, we used a permutation searching strategy to find the optimal MODIS band combinations (b1-b4 indicate MODIS bands) with the highest correlation coefficient.

Spectral indices	General form	Calibrated bands (nm)	correlation coefficients	Model form	R <sup>2</sup>	R <sup>2</sup> (log)	MRD (%)	URMSD (%)	MedRatio
2 bands	$R_{rs,b1} - R_{rs,b2}$	488, 748	-0.63	1	0.40	0.34	33.44	36.01	1.09
	$R_{rs,b1} + R_{rs,b2}$	469, 488	-0.54	2	0.47	0.35	34.69	37.78	1.04
	$R_{rs,b1}/R_{rs,b2}$	645, 667	0.54	2	0.34	0.27	39.87	41.25	1.11
	$(R_{rs,b1} - R_{rs,b2})/(R_{rs,b1} + R_{rs,b2})$	645, 667	0.52	1	0.34	0.27	40.02	40.71	1.11
	$(R_{rs,b1} + R_{rs,b2}) \times R_{rs,b3}$	488, 678	-0.60	3	0.38	0.21	33.54	36.16	1.04
3 bands	$(1/R_{rs,b1} - 1/R_{rs,b2}) \times R_{rs,b3}$	443, 531, 555	0.55	2	0.31	0.20	43.90	43.21	1.17
	$(R_{rs,b1} - R_{rs,b2}) \times R_{rs,b3}$	412, 469, 488	0.48	3	0.25	0.07	45.89	47.65	1.09
	$(1/R_{rs,b1} - 1/R_{rs,b2}) \times (1/R_{rs,b3} - 1/R_{rs,b2})$	547, 555, 645	0.65	4	0.42	0.29	38.74	41.57	1.12
	$R_{rs,b1}/R_{rs,b2} + R_{rs,b3}$	547, 555, 645	-0.57	3	0.32	0.11	43.49	45.11	1.07
	$R_{rs,b1}/(R_{rs,b2} + R_{rs,b3})$	469, 488, 531	-0.49	1	0.32	0.25	42.63	42.88	1.14
	$R_{rs,b2} - (R_{rs,b1} + (R_{rs,b3} - R_{rs,b1}) \times (b2 - b1)/(b3 - b1))$	412, 443, 645	-0.70	4	0.50	0.48	32.96	29.93	0.93
	$(R_{rs,b1} - R_{rs,b2})/(R_{rs,b3} - R_{rs,b4})$	412, 443, 469, 531	-0.69	3	0.48	0.44	33.03	33.54	1.12
4 bands	$(1/R_{rs,b1} - 1/R_{rs,b2})/(1/R_{rs,b3} - 1/R_{rs,b4})$	412, 443, 469, 531	-0.60	4	0.41	0.41	35.91	36.55	1.11
	$R_{rs,b1}/R_{rs,b2} + R_{rs,b3}/R_{rs,b4}$	412, 443, 645, 667	0.65	4	0.43	0.38	38.08	39.20	1.12
	$(R_{rs,b1} + R_{rs,b2})/(R_{rs,b3} + R_{rs,b4})$	469, 488, 531, 547	-0.47	1	0.30	0.21	45.05	46.28	1.15

Model form 1:  $y = a \cdot \exp(b \cdot x)$ ; Model form 2:  $y = a \cdot x^b$ ; Model form 3:  $y = a \cdot x + b$ ; Model form 4:  $y = a \cdot x^2 + b \cdot x + c$ .

URMSD was to avoid the impact of outliers causing skewed error distributions (Hu et al., 2012). The calculations of MRD, URMSD, and MedRatio are described as follows:

$$\text{MRD} = \text{median} \left( \frac{E_i - M_i}{M_i} \right) \quad (2)$$

$$\text{URMSD} = \sqrt{2 \cdot \text{median} \left( \frac{(E_i - M_i)^2}{E_i + M_i} \right)} \quad (3)$$

$$\text{MedRatio} = \text{median} \left( \frac{E_i}{M_i} \right) \quad (4)$$

where  $E_i, M_i$  are the estimated and *in situ* measured Chl-*a*, respectively, and  $n$  is the number of matched pairs.

### 3.3. Determination of the spatial and temporal dynamics of Chl-*a*

The proposed Chl-*a* algorithm was applied to 5879 MODIS images from 2003 to 2019 to generate long-term Chl-*a* records for coastal waters in the GBA. For each image, Chl-*a* retrievals for pixels less than three pixels away from the coastline were removed to eliminate the potential impacts of land adjacent effects (Feng and Hu, 2017). The daily MODIS Chl-*a* maps were used to generate monthly mean Chl-*a* composites, which were used further to produce annual mean and climatological monthly mean Chl-*a* maps. There are some missing values due to several factors (e.g., cloud, sunglint, and land), and at least six and three valid Chl-*a* values are required for the calculation of annual mean and climatological monthly mean, respectively. Trends (also as change rate) for each location of the study region were calculated and represented the linear slope over the annual mean Chl-*a* maps, following the same methods as many previous studies (Guan et al., 2020; Wang et al., 2021; Yung et al., 2001).

## 4. Results

### 4.1. Developing a hybrid Chl-*a* algorithm with *in situ* datasets

The recalibrated OC3 algorithm (hereafter simply “OC3” unless otherwise specified) shows the best agreement between *in situ*  $R_{rs}$ -estimated and field-measured Chl-*a* among the examined algorithms, with

the lowest MRD and URMSD and the highest R<sup>2</sup> (Fig. 4a, b & c, and Table 2). The accuracy levels of all algorithms (including OC3) show an apparent decreasing trend with increasing water turbidity (i.e.,  $R_{rs,645}$ ). A Thres- $R_{rs,645}$  value of 0.006 can be determined, as Chl-*a* can be accurately estimated with the OC3 algorithm when  $R_{rs,645}$  is below 0.006. The selection of this critical value is a compromise between the performance of the algorithm (i.e., unacceptable accuracy levels when  $R_{rs,645} > 0.006$ , with R<sup>2</sup> < 0.4 and median ratio > 1.1), the coverage of the Chl-*a* and turbidity levels (i.e., Chl-*a* is ~ 33 µg/L and TSS is ~ 5 mg/L for  $R_{rs,645} = 0.006$ , see Figure S2), and the number of data used in algorithm development (i.e., >300 *in situ*  $R_{rs}$ -Chl-*a* pairs for  $R_{rs,645} < 0.006$ ). The recalibrated OC3 algorithm can be expressed as follows:

$$\text{Chl}_{OC3} = 10^{(ax^4 + bx^3 + cx^2 + dx + e)} \quad (5)$$

where  $x = \log \left( \frac{\max(R_{rs,443}, R_{rs,488})}{R_{rs,547}} \right)$ . The recalibrated coefficients from  $a$  to  $e$  are -4.021, 0.132, 2.235, -2.615, and 0.234, respectively.

Of the various band combinations designed for turbid waters (see Table 3), a baseline-based index (denoted as BL443) showed the best performance, which can be expressed as follows:

$$\text{BL443} = R_{rs,443} - \left( R_{rs,412} + \frac{443 - 412}{645 - 412} (R_{rs,645} - R_{rs,412}) \right) \quad (6)$$

The designation of BL443 is very similar to that of CI, FAI, FLH, MCI, and many spectral indices (Hu, 2009; Hu et al., 2012; Letelier and Abbott, 1996; McCullough, 2007; Shen et al., 2010), which numerically represents the heights of the reflectance at the central band above a baseline linking the reflectance at short and long wavelengths (Fig. 5). As shown in Fig. 5a, the short, central, and long wavelengths used in BL443 are 413, 443 and 645 nm, respectively.

Similar to the OC3 algorithm, the performance of the BL443-based algorithm is also sensitive to turbidity changes (Fig. 4). The best agreement between the estimated and measured Chl-*a* was found when  $R_{rs,645}$  was approximately 0.006; the performance was substantially more unsatisfactory when  $R_{rs,645}$  was below this threshold (Fig. 4d&e).

To follow the convention adopted by NASA in determining the coefficients for OCx algorithms (Hu et al., 2019), we binned the data according to different levels of Chl-*a* and  $R_{rs,645}$  (598 in total for pairs with  $R_{rs,645}$  above 0.006). Chl-*a* data were first binned in logarithmic space (Eq. (7)), and the corresponding mean BL443 was calculated for each

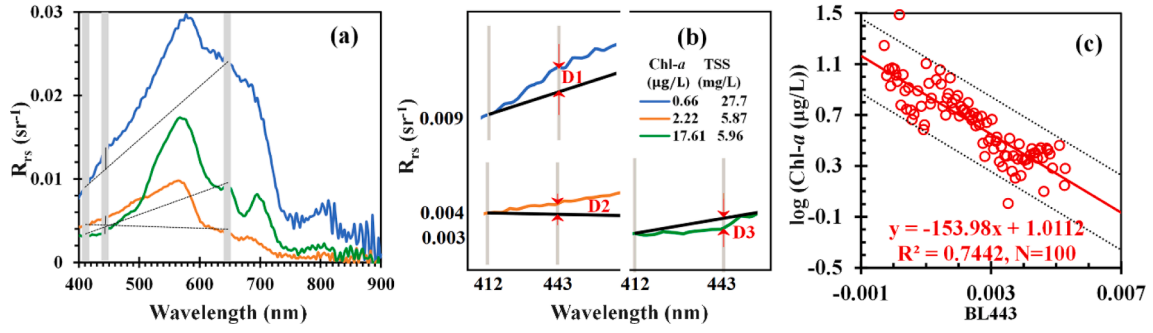


**Fig. 5.** (a-b) Comparison of several *in situ*  $R_{rs}$  records ( $\text{sr}^{-1}$ ) with different Chl-*a* concentrations ( $\mu\text{g/L}$ ). The heights of the 443-nm band above the baseline linking the reflectance at 412- and 645-nm bands (BL443, denoted as  $D_i$  of (b)) decrease with elevated Chl-*a*. (c) Relationship between binned BL443 and Chl-*a*.

log-space grid. Then, the binned data were binned again according to BL443 in linear space (Eq. (8)), with the corresponding mean Chl-*a* and mean BL443 calculated.

$$L_{Chl,a,i} = 0.01 \times i^{1.01}, H_{Chl,a,i} = 0.01 \times (i+1)^{1.01}, i = 1, 2, \dots, N \quad (7)$$

$$L_{BL443,i} = min + \Delta \times (i-1), H_{BL443,i} = min + \Delta \times i, i = 1, 2, \dots, N \quad (8)$$

where  $L_{Chl,a,i}$  and  $H_{Chl,a,i}$  are the lower and higher bounds for the  $i^{\text{th}}$  Chl-*a* bin.  $L_{BL443,i}$ ,  $H_{BL443,i}$  are the lower and higher bounds for the  $i^{\text{th}}$  bin of BL443,  $\Delta$  is the fixed interval and  $min$  is the minimum value of the first-binned value of BL443. The coefficients of the algorithm were determined through the regression between the binned Chl-*a* and BL443 (Fig. 5c), which can be expressed as follows:

$$Chl_{BL443} = 10^{ax+b} \quad (9)$$

where  $a = -173.16$ ,  $b = 0.9647$  ( $R^2 = 0.74$ ).

Since  $R_{rs,645} = 0.006$  is the same upper bound that the OC3 algorithm shows for optimal retrieval accuracies in the study area in lower turbidity waters, a hybrid algorithm based on the OC3 and BL443-based algorithms is developed to retrieve Chl-*a* across the entire *in situ* measured turbidity range. The hybrid algorithm is formulated as follows:

$$Chl - a = \begin{cases} Chl_{OC3} [R_{rs,645} \leq 0.005] \\ Chl_{BL443} [R_{rs,645} > 0.007] \\ \alpha Chl_{OC3} + \beta Chl_{BL443} [0.005 < R_{rs,645} \leq 0.007] \end{cases} \quad (10)$$

where the weighting factors are  $\alpha = (0.007 - R_{rs,645}) / (0.007 - 0.005)$ ,  $\beta = (R_{rs,645} - 0.005) / (0.007 - 0.005)$ . Here, we select 0.005 and 0.007 as the lower and upper bounds of the transition zone, respectively, which are used to ensure a smooth transition between the

OC3 and BL443 algorithms. The overall accuracy measures of the hybrid algorithm are presented in Fig. 6a and Table 4.

#### 4.2. Performance of satellite-derived Chl-*a* using the hybrid algorithm

Validation using satellite-*in situ* match-up pairs shows that Chl-*a* concentrations estimated using the hybrid algorithm agree well with the *in situ* measurements ( $R^2 = 0.81$ ) (Fig. 6b); the matched points are generally distributed along the 1:1 line with the slope of 0.73. The URMSD was 33.8% ( $N = 255$ ) and was reduced to 23.5% when only the datasets from our group were used (i.e., excluding the HKEPD dataset,  $N = 117$ ). Indeed, such an accuracy level satisfied the mission goal of the ocean color community in obtaining Chl-*a* concentrations (i.e., an uncertainty level of 35% for the global ocean) (O'Reilly and Werdell, 2019). Furthermore, we found reasonable agreement between *in situ* Chl-*a* and satellite retrievals across four seasons (see Fig. 6b), with the slopes of 1.036 (Spring), 0.6475 (Summer), 0.8387 (Autumn), and 0.7817 (Winter), respectively. The slope difference across four seasons is partially due to the seasonal dynamics of phytoplankton community composition (or photoacclimation status) and the seasonal difference in the terrestrial discharges. These results indicate that the currently developed hybrid algorithm can be used to estimate long-term Chl-*a* patterns of the coastal oceans in the GBA and across different seasons.

#### 4.3. Intra- and interannual dynamics of Chl-*a*

Fig. 7 shows the climatological monthly mean Chl-*a* maps from 2003 to 2019. Although Chl-*a* concentrations consistently decreased from the northwestern to southeastern GBA throughout the year, spatial patterns diverged substantially between dry and wet seasons. For nearshore waters, higher Chl-*a* concentrations (red colors) could be observed during wet seasons (April to September) than during dry seasons

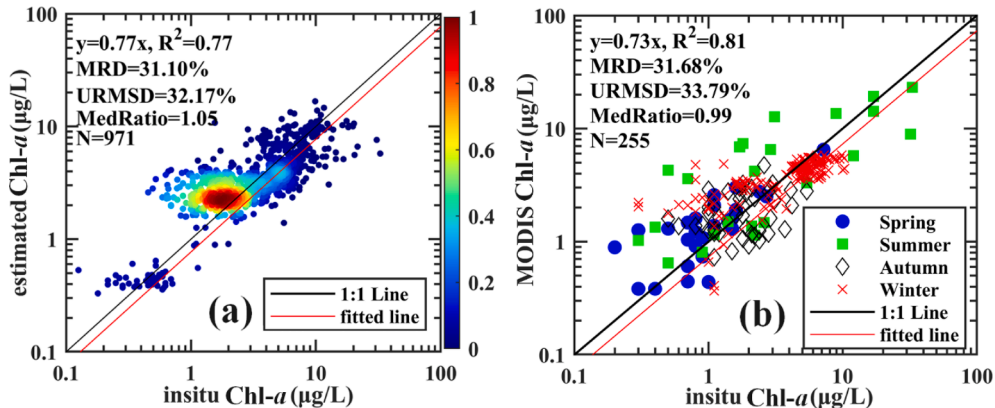


**Fig. 6.** (a) Overall performance of the proposed model gauged by *in situ*  $R_{rs}$ -retrieved Chl-*a* datasets, where color indicates the density of data points. (b) Validation of MODIS-retrieved Chl-*a* concentrations using *in situ* Chl-*a* data obtained from three cruises and routine surveys by HKEPD.

**Table 4**

Overall performance of the proposed model in this study based on 971 *in situ*  $R_{rs}$ -Chl-*a* samples. Comparisons with previous studies over this study area are also indicated.

Model	$x$	Model form	$R^2$	$R^2(\log)$	MRD (%)	URMSD (%)	MedRatio
This study			0.46	0.60	31.10	32.17	1.05
Liu_2008	$x = \frac{R_{rs}(695) - R_{rs}(694)}{695 - 694}$	$Chla = 6.1826 + 40833.1121x + 89521596.0545x^2 - 51080584539.5196x^3$	0.00	0.00	60.84	64.00	1.43
Liu_2010	$x = \frac{R_{rs}(859)}{R_{rs}(645)}$	$Chl - a = 5.9278e^{7.4727x}$	0.00	0.01	420.54	139.05	5.21
Chen_2011	$x = \left( \frac{1}{R_{rs}(684)} - \frac{1}{R_{rs}(690)} \right) \times R_{rs}(718)$	$Chla = 331.01x + 14.609$	0.14	0.03	201.91	111.70	2.22
Zhang_2011	$x = \frac{R_{rs}(748)}{R_{rs}(667)}$	$Chl - a = \exp\left(\frac{x - 0.4016}{0.1208}\right)$	0.01	0.02	93.62	171.58	0.08
Majid_2016	$x = \frac{R_{rs}(660)}{R_{rs}(485)^2}$	$y = 1.31 + 0.64x$	0.37	0.30	947.48	165.14	10.47

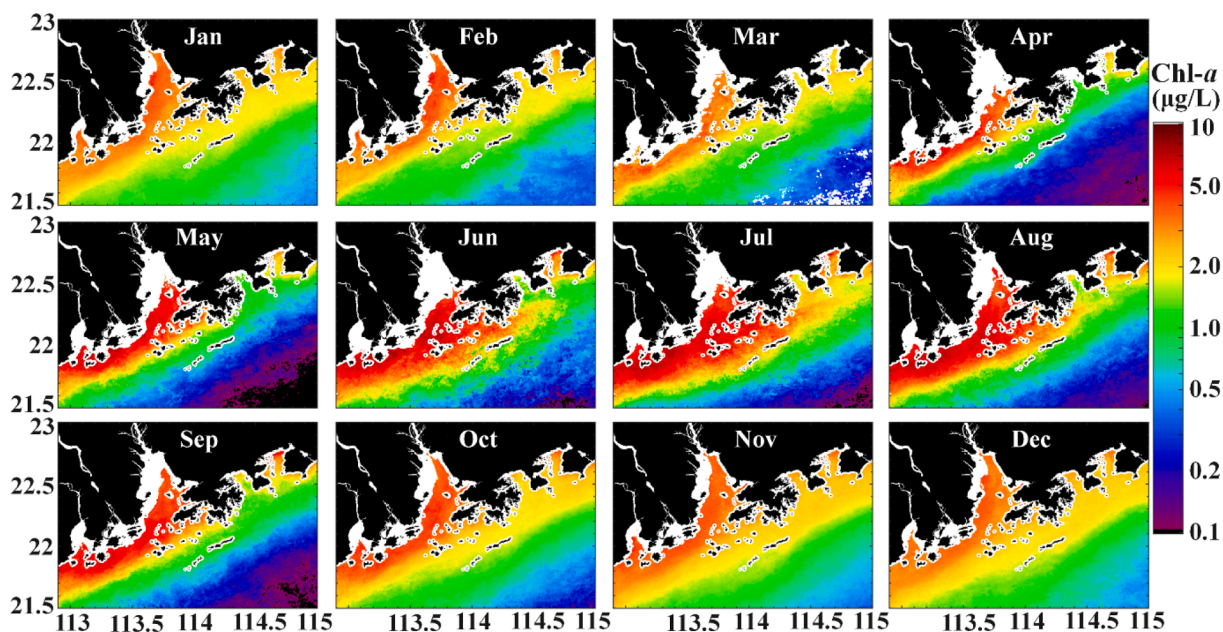


**Fig. 7.** Climatological monthly Chl-*a* distributions from MODIS (2003–2019). For all pixels, at least three valid monthly data in all years were required for the climatological monthly mean calculation. Black and white areas denote land and nonretrievals, respectively.

(October to March). In particular, large plumes can be identified in the summer months in the study area, which could be attributed to larger riverine discharge and the prevailing monsoon-driven coastal current (Ye et al., 2020). In contrast, Chl-*a* decreased remarkably when the dry season started (October) and then remained low through March of the following year. For offshore waters, opposite intra-annual variations were observed, with higher Chl-*a* values in the dry season than in the wet season.

The annual mean Chl-*a* maps from 2003 to 2019 are shown in Fig. 8, where the spatial patterns are similar to that of the monthly composite (Fig. 7), with higher values in the northwestern areas of the coastal oceans in the GBA. Fig. 9 demonstrates the change rate of Chl-*a* concentration within the 17-year period, where the color-coded regions show statistically significant trends (i.e.,  $p < 0.05$ ). The Chl-*a* of the west coastal waters in the GBA shows a dominant decreasing trend (averaged at  $0.054 \mu\text{g/L yr}^{-1}$ ) during the observational period, particularly in the inner PRE, where riverine discharge and saltwater interact frequently. In contrast, significant increasing trends primarily occurred in the eastern DYB (averaged at  $0.035 \mu\text{g/L yr}^{-1}$ ), located east of the study area. Few regions in offshore oceans show significantly changing trends, and their change rates are very low, indicating a generally stable Chl-*a* level during the study period.

## 5. Discussion

### 5.1. Uncertainty in the MODIS Chl-*a* concentrations

We proposed a novel hybrid Chl-*a* algorithm for the coastal oceans of the GBA, where the recalibrated OC3 and a baseline-based index (BL443) algorithms were used for low- and high-turbidity waters, respectively, and the  $R_{rs,645}$  was used to determine the turbidity level. OC3 is based on the ratio between blue and green wavelengths, which is the default algorithm for MODIS band adopted by NASA to generate the Chl-*a* product with values not-less-than  $0.3 \mu\text{g/L}$  (Hu et al., 2012); our results demonstrate its applicability in low-turbidity waters in the GBA. However, the absorption of phytoplankton pigments in the blue band overlaps with other optically active parameters (e.g., dissolved organic matter and suspended inorganic particles), making it difficult to estimate Chl-*a* in coastal waters enriched in those parameters with the OC3 algorithm (e.g., Moore et al., 2014). Thus, we proposed a baseline algorithm (BL443) based on the high correlation ( $\sim 0.7$ ) between BL443 and Chl-*a* in turbid waters in our study region, and this algorithm outperformed various types of spectral indices that were previously used to estimate Chl-*a* in global coastal and open oceanic waters (see Table 3). The subtraction-based designation of baseline indices has been

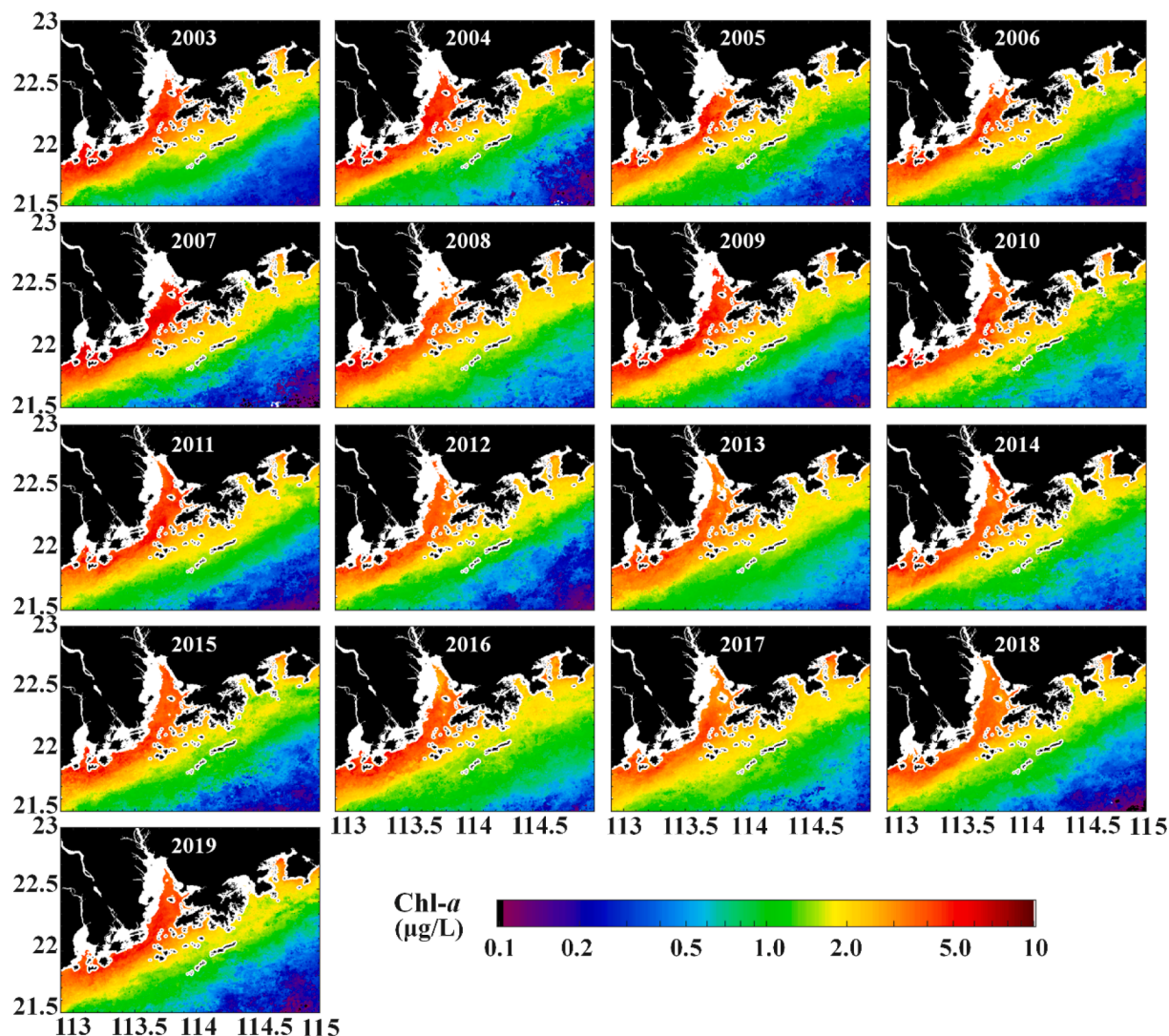


Fig. 8. Annual Chl-a distributions from MODIS (2003–2019). For all pixels, at least six valid monthly values were required for the annual mean calculation. Black and white areas denote land and nonretrievals, respectively.

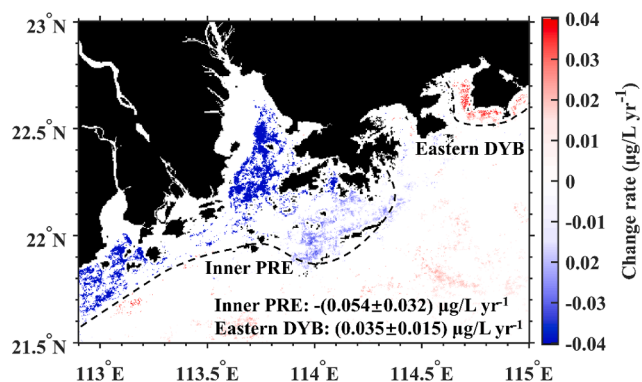


Fig. 9. The change rate ( $\mu\text{g/L yr}^{-1}$ ) of Chl-a, expressed as the linear slope that was estimated using the annual maps in Fig. 8; only the locations with significant trends ( $p < 0.05$ ) are color-coded. Significant decreasing and increasing trends are detected in the inner Pearl River Estuary (inner PRE) and eastern Daya Bay (eastern DYB), respectively.

demonstrated to be more tolerant of atmospheric correction uncertainties, satellite/solar geometries, and other unfavorable observational conditions (Hu, 2009; Hu et al., 2012).

We also used our datasets to examine the performance of regional Chl-a algorithms (i.e., Liu\_2008, Liu\_2010, Chen\_2011, Zhang\_2011, Majid\_2016, named after the authors and published years) that were previously developed for the same study area. Unfortunately, none of these algorithms can obtain promising Chl-a retrievals (see Table 4), possibly due to the limited datasets used to establish these algorithms. Indeed, validations show that the MODIS-derived Chl-a concentration has a URMSD of 33.8%. However, such uncertainties cannot be attributed to only the hybrid algorithm for the following three reasons. First, bias induced by imperfect atmospheric correction algorithm to  $R_{rs}$  produced uncertainty of retrieved Chl-a. Second, the *in situ* data are point-based observations, mismatching the area-based measurements by satellite (i.e.,  $250 \times 250$  m for MODIS). Third, time windows (3 h for our surveyed data and 1 day for the HKEPD datasets) were used to determine the *in situ*-satellite match-ups, and the changes in the optical properties within the time windows may also lead to the resulting uncertainty in the calculations. This argument can be partially justified by the fact that

the uncertainty estimate using our surveyed data (23.5%), with a smaller time window, is lower than that using HKEPD data (50.1%) or using the two datasets (33.8%). Nevertheless, we acknowledge that the Chl-*a* algorithm developed here was based on our own *in situ* data, while its applicability to other coastal and estuarine regions requires further regionalized recalibrations.

## 5.2. Implications and limitations

Eutrophication is a big concern in coastal waters as it can affect not only aquatic ecosystem health and marine fishery yield but also threaten adjacent water supplies. Indeed, the coastal water of the GBA provides a large-scale living environment for aquaculture. As reported, the marine fishery yield occupies 45% of the total fishery industry in Guangdong province (numbers were estimated from the Chinese Fishery Statistical Yearbook (2019)). Moreover, limited by terrestrial surface freshwater resources, coastal brackish or salty water as well as coastal groundwater often exchanged with intrusive seawater have been becoming an indispensable resource within the water supply system of surrounding cities and counties (Liu et al., 2019a; Liu et al., 2019b). As an important indicator of eutrophication state, accurate Chl-*a* monitoring and its interannual changes during recent decades can serve as baseline information for estuary-specific environmental assessment and sustainable management. The developed local Chl-*a* retrieval algorithm could be operationally applied for real-time monitoring of water quality and water security based on the frequent MODIS observations in the future. Clarifying the long-term changes of Chl-*a* would help the government enact policies for local conditions.

The growth rate of phytoplankton in the surface ocean can be modulated by temperature, light availability, and nutrients, among many other environmental factors (Arteaga et al., 2020; Rabalais et al., 2009; Sherman et al., 2016). Meanwhile, these factors can be further regulated by local climate, regional physical processes, and anthropogenic activities. As such, a future quantitative attribution of the Chl-*a* changes over the coastal oceans of the GBA requires not only detailed datasets of all environmental factors, but also sophisticated numerical models to understand the biophysical process of this region.

## 6. Conclusions

We proposed a hybrid Chl-*a* algorithm for the coastal oceans of the GBA in China. In this algorithm, the OC3 algorithm and a baseline index (BL443) were adopted for low- and high-turbidity waters, and  $R_{rs,645} = 0.006$  was used to determine the water turbidity types. Validations show that satellite Chl-*a* retrieved using this algorithm has an uncertainty level of 33.8%. We applied this hybrid algorithm to all MODIS images between 2003 and 2019 covering the GBA and provided the first comprehensive characterization of the Chl-*a* dynamics in this region. In addition to the remarkable seasonality, the most striking finding is the significant decreasing trend in the inner estuary areas and the increasing trends in Daya Bay. Our study provides important baseline information for future protection and mitigation efforts for regional coastal oceans; the methods developed here are easily extended to other coastal global estuarine waters to examine the long-term patterns of phytoplankton dynamics.

## CRediT authorship contribution statement

**Yan Tong:** Methodology, Software, Validation, Formal analysis, Writing – original draft. **Lian Feng:** Conceptualization, Supervision, Writing – review & editing, Funding acquisition. **Dan Zhao:** Data curation. **Wang Xu:** Data curation. **Chunmiao Zheng:** Funding acquisition.

## Declaration of Competing Interest

The authors declare that they have no known competing financial interests or personal relationships that could have appeared to influence the work reported in this paper.

## Acknowledgement

This research was supported by the National Natural Science Foundation of China (Grant#: 41890851, 41890852 and 41971304) and the Shenzhen Science and Technology Innovation Committee (JCYJ20190809155205559). The authors want to thank the United States Geological Survey (USGS) for providing SeaDAS software (<https://seadas.gsfc.nasa.gov/>), MODIS data (<https://oceancolor.gsfc.nasa.gov/>). Three anonymous reviewers provided thoughtful comments and suggestions to help improve this manuscript, which are highly appreciated.

## Appendix A. Supplementary data

Supplementary data to this article can be found online at <https://doi.org/10.1016/j.jag.2022.102922>.

## References

- Arabi, B., Salama, M.S., Pitarch, J., Verhoef, W., 2020. Integration of in-situ and multi-sensor satellite observations for long-term water quality monitoring in coastal areas. *Remote Sens. Environ.* 239, 111632.
- Arteaga, L.A., Boss, E., Behrenfeld, M.J., Westberry, T.K., Sarmiento, J.L., 2020. Seasonal modulation of phytoplankton biomass in the Southern Ocean. *Nat. Commun.* 11 (1), 1–10.
- Boyce, D.G., Lewis, M.R., Worm, B., 2010. Global phytoplankton decline over the past century. *Nature* 466 (7306), 591–596.
- Breitburg, D., Levin, L.A., Oschlies, A., Grégoire, M., Chavez, F.P., Conley, D.J., Garçon, V., Gilbert, D., Gutiérrez, D., Isensee, K., Jacinto, G.S., Limburg, K.E., Montes, I., Naqvi, S.W.A., Pitcher, G.C., Rabalais, N.N., Roman, M.R., Rose, K.A., Seibel, B.A., Telszewski, M., Yasuhara, M., Zhang, J., 2018. Declining oxygen in the global ocean and coastal waters. *Science* 359 (6371).
- Chen, S., Fang, L., Li, H., Chen, W., Huang, W., 2011. Evaluation of a three-band model for estimating chlorophyll-*a* concentration in tidal reaches of the Pearl River Estuary, China. *ISPRS J. Photogramm. Remote Sens.* 66 (3), 356–364.
- Cheng, K., Chan, S.N., Lee, J.H., 2020. Remote sensing of coastal algal blooms using unmanned aerial vehicles (UAVs). *Mar. Pollut. Bull.* 152, 110889.
- Feng, L., Hu, C., 2017. Land adjacency effects on MODIS *a*qua top-of-atmosphere radiance in the shortwave infrared: S statistical assessment and correction. *J. Geophys. Res. Oceans* 122 (6), 4802–4818.
- Fu, Q., He, Y., Feng, Y., Qin, Y., Yin, B., 2015. A semi-analytical model of chlorophyll-*a* concentration in Pear River Estuary under various tidal conditions. *IEEE*, pp. 1–8.
- Gitelson, A.A., Dall'Olmo, G., Moses, W., Rundquist, D.C., Barrow, T., Fisher, T.R., Gurlin, D., Holz, J., 2008. A simple semi-analytical model for remote estimation of chlorophyll-*a* in turbid waters: Validation. *Remote Sens. Environ.* 112 (9), 3582–3593.
- Gitelson, A.A., Schalles, J.F., Hladik, C.M., 2007. Remote chlorophyll-*a* retrieval in turbid, productive estuaries: Chesapeake Bay case study. *Remote Sens. Environ.* 109 (4), 464–472.
- Gohin, F., Van der Zande, D., Tilstone, G., Eleveld, M.A., Lefebvre, A., Andrieux-Loyer, F., Blauw, A.N., Bryère, P., Devreker, D., Garnesson, P., 2019. Twenty years of satellite and in situ observations of surface chlorophyll-*a* from the northern Bay of Biscay to the eastern English Channel. Is the water quality improving? *Remote Sens. Environ.* 233, 111343.
- Guan, Q., Feng, L., Hou, X., Schurgers, G., Zheng, Y., Tang, J., 2020. Eutrophication changes in fifty large lakes on the Yangtze Plain of China derived from MERIS and OLCI observations. *Remote Sens. Environ.* 246, 111890.
- Hafeez, S., Wong, M.S., Ho, H.C., Nazeer, M., Nichol, J., Abbas, S., Tang, D., Lee, K.H., Pun, L., 2019. Comparison of machine learning algorithms for retrieval of water quality indicators in case-II waters: a case study of Hong Kong. *Remote Sensing* 11 (6), 617.
- Harrison, P.J., Yin, K., Lee, J.H.W., Gan, J., Liu, H., 2008. Physical–biological coupling in the Pearl River Estuary. *Cont. Shelf Res.* 28 (12), 1405–1415.
- Hu, C., 2009. A novel ocean color index to detect floating algae in the global oceans. *Remote Sens. Environ.* 113 (10), 2118–2129.
- Hu, C., Chen, Z., Clayton, T.D., Swarzenski, P., Brock, J.C., Muller-Karger, F.E., 2004. Assessment of estuarine water-quality indicators using MODIS medium-resolution bands: Initial results from Tampa Bay, FL. *Remote Sensing of Environment* 93 (3), 423–441.
- Hu, C., Feng, L., Lee, Z., Franz, B.A., Bailey, S.W., Werdell, P.J., Proctor, C.W., 2019. Improving satellite global chlorophyll *a* data products through algorithm refinement and data recovery. *J. Geophys. Res. Oceans* 124 (3), 1524–1543.

- Hu, C., Lee, Z., Franz, B., 2012. Chlorophyll algorithms for oligotrophic oceans: A novel approach based on three-band reflectance difference. *J. Geophys. Res. Oceans* 117 (C1).
- Hu, W., Lo, W., Chua, H., Sin, S., Yu, P., 2001. Nutrient release and sediment oxygen demand in a eutrophic land-locked embayment in Hong Kong. *Environ. Int.* 26 (5–6), 369–375.
- Le, C., Hu, C., English, D., Cannizzaro, J., Kovach, C., 2013. Climate-driven chlorophyll-a changes in a turbid estuary: Observations from satellites and implications for management. *Remote Sens. Environ.* 130, 11–24.
- Lee, Z., Carder, K.L., Arnone, R.A., 2002. Deriving inherent optical properties from water color: a multiband quasi-analytical algorithm for optically deep waters. *Appl. Opt.* 41 (27), 5755–5772.
- Letelier, R.M., Abbott, M.R., 1996. An analysis of chlorophyll fluorescence algorithms for the Moderate Resolution Imaging Spectrometer (MODIS). *Remote Sens. Environ.* 58 (2), 215–223.
- Li, D., Gan, J., Hui, R., Liu, Z., Yu, L., Lu, Z. and Dai, M. 2020. Vortex and biogeochemical dynamics for the hypoxia formation within the coastal transition zone off the Pearl River Estuary. *Journal of Geophysical Research: Oceans* 125(8), e2020JC016178.
- Li, J., Gao, M., Feng, L., Zhao, H., Shen, Q., Zhang, F., Wang, S., Zhang, B., 2019. Estimation of chlorophyll-a concentrations in a highly turbid eutrophic lake using a classification-based MODIS land-band algorithm. *IEEE J. Sel. Top. Appl. Earth Obs. Remote Sens.* 12 (10), 3769–3783.
- Liu, B., Peng, S., Liao, Y., Wang, H., 2019a. The characteristics and causes of increasingly severe saltwater intrusion in Pearl River Estuary. *Estuar. Coast. Shelf Sci.* 220, 54–63.
- Liu, D.-Z., Tang, S., Fu, D.-Y., 2008. Study on retrieval of chlorophyll a concentration in the waters of Pearl River Estuary by hyperspectral technology. *Journal of Guangdong Ocean University* 28 (1), 49–52.
- Liu, D., Chen, C., Gong, J., Fu, D., 2010. Remote sensing of chlorophyll-a concentrations of the Pearl River Estuary from MODIS land bands. *Int. J. Remote Sens.* 31 (17–18), 4625–4633.
- Liu, F., Tang, S., 2019. Evaluation of red-peak algorithms for chlorophyll measurement in the Pearl River Estuary. *IEEE Trans. Geosci. Remote Sens.* 57 (11), 8928–8936.
- Liu, X., Dai, J., Ng, T.-L., Chen, G., 2019b. Evaluation of potential environmental benefits from seawater toilet flushing. *Water Res.* 162, 505–515.
- Lu, Z., Gan, J., Dai, M., Liu, H., Zhao, X., 2018. Joint effects of extrinsic biophysical fluxes and intrinsic hydrodynamics on the formation of hypoxia west off the Pearl River Estuary. *J. Geophys. Res. Oceans* 123 (9), 6241–6259.
- Lu, Z., Gan, J., Dai, M., Zhao, X., Hui, C.R., 2020. Nutrient transport and dynamics in the South China Sea: A modeling study. *Prog. Oceanogr.* 183, 102308.
- Matthews, M.W., 2011. A current review of empirical procedures of remote sensing in inland and near-coastal transitional waters. *Int. J. Remote Sens.* 32 (21), 6855–6899.
- McCullough, G. 2007 *MERIS/MODIS prediction of chlorophyll in Lake Winnipeg*, Canadian Department of Fisheries and Oceans Institute of Ocean Sciences ....
- Mobley, C.D., 1999. Estimation of the remote-sensing reflectance from above-surface measurements. *Appl. Opt.* 38 (36), 7442–7455.
- Moore, T.S., Dowell, M.D., Bradt, S., Verdu, A.R., 2014. An optical water type framework for selecting and blending retrievals from bio-optical algorithms in lakes and coastal waters. *Remote Sens. Environ.* 143, 97–111.
- Nazeer, M., Nichol, J.E., 2016. Development and application of a remote sensing-based Chlorophyll-a concentration prediction model for complex coastal waters of Hong Kong. *J. Hydrol.* 532, 80–89.
- Neil, C., Spyarakos, E., Hunter, P.D., Tyler, A.N., 2019. A global approach for chlorophyll-a retrieval across optically complex inland waters based on optical water types. *Remote Sens. Environ.* 229, 159–178.
- Neumann, B., Vafeidis, A.T., Zimmermann, J., Nicholls, R.J., 2015. Future coastal population growth and exposure to sea-level rise and coastal flooding—a global assessment. *PLoS ONE* 10 (3), e0118571.
- Ning, X.-R., Chai, F., Xue, H., Cai, Y., Liu, C., Shi, J., 2004. Physical-biological oceanographic coupling influencing phytoplankton and primary production in the South China Sea. *J. Geophys. Res. Oceans* 109 (C10).
- O'Reilly, J.E., Werdell, P.J., 2019. Chlorophyll algorithms for ocean color sensors-OC4, OC5 & OC6. *Remote Sens. Environ.* 229, 32–47.
- Odermatt, D., Danne, O., Philipson, P., Brockmann, C., 2018. Diversity II water quality parameters from ENVISAT (2002–2012): a new global information source for lakes. *Earth Syst. Sci. Data* 10 (3), 1527–1549.
- Odermatt, D., Gitelson, A., Brando, V.E., Schaepman, M., 2012. Review of constituent retrieval in optically deep and complex waters from satellite imagery. *Remote Sens. Environ.* 118, 116–126.
- Ondrusek, M., Stengel, E., Kinkade, C.S., Vogel, R.L., Keegstra, P., Hunter, C., Kim, C., 2012. The development of a new optical total suspended matter algorithm for the Chesapeake Bay. *Remote Sens. Environ.* 119, 243–254.
- Qiu, D., Zhong, Y., Chen, Y., Tan, Y., Song, X., Huang, L., 2019. Short-term phytoplankton dynamics during typhoon season in and near the Pearl River Estuary, South China Sea. *J. Geophys. Res. Biogeosci.* 124 (2), 274–292.
- Rabalais, N.N., Turner, R.E., Diaz, R.J., Justic, D., 2009. Global change and eutrophication of coastal waters. *ICES J. Mar. Sci.* 66 (7), 1528–1537.
- Shen, F., Zhou, Y.-X., Li, D.-J., Zhu, W.-J., Suhyb Salama, M., 2010. Medium resolution imaging spectrometer (MERIS) estimation of chlorophyll-a concentration in the turbid sediment-laden waters of the Changjiang (Yangtze) Estuary. *Int. J. Remote Sens.* 31 (17–18), 4635–4650.
- Sherman, E., Moore, J.K., Primeau, F., Tanouye, D., 2016. Temperature influence on phytoplankton community growth rates. *Global Biogeochem. Cycles* 30 (4), 550–559.
- Strokal, M., Yang, H., Zhang, Y., Kroeze, C., Li, L., Luan, S., Wang, H., Yang, S., Zhang, Y., 2014. Increasing eutrophication in the coastal seas of China from 1970 to 2050. *Mar. Pollut. Bull.* 85 (1), 123–140.
- Vanhellemont, Q., Ruddick, K., 2015. Advantages of high quality SWIR bands for ocean colour processing: Examples from Landsat-8. *Remote Sens. Environ.* 161, 89–106.
- Wang, J., Tong, Y., Feng, L., Zhao, D., Zheng, C. and Tang, J. 2021. Satellite-Observed Decreases in Water Turbidity in the Pearl River Estuary: Potential Linkage With Sea-Level Rise. *Journal of Geophysical Research: Oceans* 126(4), e2020JC016842.
- Wang, M., Shi, W., 2006. Cloud masking for ocean color data processing in the coastal regions. *IEEE Trans. Geosci. Remote Sens.* 44 (11), 3196–3210.
- Wang, M., Shi, W., 2007. The NIR-SWIR combined atmospheric correction approach for MODIS ocean color data processing. *Opt. Express* 15 (24), 15722–15733.
- Wang, M., Son, S., Shi, W., 2009. Evaluation of MODIS SWIR and NIR-SWIR atmospheric correction algorithms using SeaWiFS data. *Remote Sens. Environ.* 113 (3), 635–644.
- Wang, Y.-S., Lou, Z.-P., Sun, C.-C., Sun, S., 2008. Ecological environment changes in Daya Bay, China, from 1982 to 2004. *Mar. Pollut. Bull.* 56 (11), 1871–1879.
- Wei, J., Lee, Z., Shang, S., 2016. A system to measure the data quality of spectral remote-sensing reflectance of aquatic environments. *J. Geophys. Res. Oceans* 121 (11), 8189–8207.
- WET Labs, I. (2008) *ECO 3-measurement sensor (triplet) user's guide. (revision O)*, WET Labs, Inc.
- Wong, L., Chen, J., Xue, H., Dong, L., Su, J., Heinke, G., 2003. A model study of the circulation in the Pearl River Estuary (PRE) and its adjacent coastal waters: 1. Simulations and comparison with observations. *J. Geophys. Res. Oceans* 108 (C5).
- Wu, Y., Zhang, J., Liu, S., Jiang, Z., Huang, X., 2018. Aerosol concentrations and atmospheric dry deposition fluxes of nutrients over Daya Bay, South China Sea. *Mar. Pollut. Bull.* 128, 106–114.
- Xiong, Y.J., Liu, J.F., 2018. Can Saltwater Intrusion Affect a Phytoplankton Community and Its Net Primary Production? A Study Based on Satellite and Field Observations. *Estuaries Coasts* 41 (8), 2317–2330.
- Xu, Y., Feng, L., Zhao, D., Lu, J., 2020. Assessment of Landsat atmospheric correction methods for water color applications using global AERONET-OC data. *Int. J. Appl. Earth Obs. Geoinf.* 93, 102192.
- Xuan, Y., Tang, C., Liu, G., Cao, Y., 2020. Carbon and nitrogen isotopic records of effects of urbanization and hydrology on particulate and sedimentary organic matter in the highly urbanized Pearl River Delta, China. *Journal of Hydrology* 591, 125565.
- Ye, H., Yang, C., Tang, S., Chen, C., 2020. The phytoplankton variability in the Pearl River estuary based on VIIRS imagery. *Cont. Shelf Res.* 207, 104228.
- Yung, Y.-K., Wong, C., Yau, K., Qian, P., 2001. Long-term changes in water quality and phytoplankton characteristics in Port Shelter, Hong Kong, from 1988–1998. *Mar. Pollut. Bull.* 42 (10), 981–992.
- Zhang, H., Cheng, W., Chen, Y., Yu, L., Gong, W., 2018. Controls on the interannual variability of hypoxia in a subtropical embayment and its adjacent waters in the Guangdong coastal upwelling system, northern South China Sea. *Ocean Dyn.* 68 (8), 923–938.
- Zhang, J., Yu, L., Li, X., Zhang, C., Shi, T., Wu, X., Yang, C., Gao, W., Li, Q., Wu, G., 2020. Exploring annual urban expansions in the Guangdong-Hong Kong-Macau Greater Bay Area: Spatiotemporal features and driving factors in 1986–2017. *Remote Sensing* 12 (16), 2615.
- Zhang, Y., Lin, H., Chen, C., Chen, L., Zhang, B., Gitelson, A.A., 2011. Estimation of chlorophyll-a concentration in estuarine waters: case study of the Pearl River estuary. *South China Sea. Environmental Research Letters* 6 (2), 024016.
- Zhang, Y., Wang, Y., Wang, Y., Xi, H., 2009. Investigating the impacts of landuse-landcover (LULC) change in the pearl river delta region on water quality in the pearl river estuary and Hong Kong's coast. *Remote Sensing* 1 (4), 1055–1064.